

Fano resonance engineering in slanted cavities with hyperbolic metamaterials

Fabio Vaianella* and Bjorn Maes

Micro- and Nanophotonic Materials Group, Faculty of Science, University of Mons, 20, place du Parc, B-7000 Mons, Belgium

(Received 13 July 2016; revised manuscript received 8 September 2016; published 28 September 2016)

We present the possibility to engineer Fano resonances using multilayered hyperbolic metamaterials. The proposed cavity designs are composed of multilayers with a central slanted part. The highly tunable resonances originate from the interference between a propagating and an evanescent mode inside the slanted section. The propagating mode can reach an extremely high effective index, making the realization of deeply subwavelength cavities possible, as small as 5 nm. The evanescent mode is rarely analyzed but plays an important role here, as its contribution determines the particular shape of the cavity characteristic. Moreover, these phenomena cannot be described using effective medium theory, and we provide a more rigorous analysis. The reported resonances are very sensitive to any structural changes and could be used for sensing applications.

DOI: [10.1103/PhysRevB.94.125442](https://doi.org/10.1103/PhysRevB.94.125442)

I. INTRODUCTION

Over the last decades the enhanced control over all aspects of light is a major research direction. As a result of the progress in nanofabrication, metamaterials have attracted a large scientific interest for their abilities to steer electromagnetic fields, thanks to a tailoring of the subwavelength features [1–7].

A particular subclass of these materials, the hyperbolic metamaterials (HMMs), presents multiple interesting properties, such as a very large density of states [8,9], an extreme refractive index, and negative refraction [10,11]. Two well-known structures with these hyperbolic properties are periodic one-dimensional multilayers (very thin metallic and dielectric layers) [12–16] and two-dimensional periodic arrays (metallic nanorods in a dielectric host) [17–19].

Various designs of cavities based on HMMs have been studied, and they present interesting features such as an anomalous scaling law [10], whispering-gallery modes [20], zeroth order Fabry-Perot resonances [21], and Fano resonances [22].

Fano resonances are asymmetrically shaped resonant phenomena that arise from the interference between a slowly varying background and a narrow resonant process [23–25]. Because their features stem from the interplay between two distinct channels, the resonances are very sensitive to any changes, rendering them interesting, among others, for sensing applications [26].

Here we propose very compact, high-quality cavities based on slanted multilayer HMMs, which present Fano resonances. Using rigorous numerical simulations and a thorough modal analysis, we elucidate the mechanism as the simultaneous excitation of a propagating and an evanescent mode. The propagating mode creates Fabry-Perot resonances, whereas the evanescent modes lead to a slowly varying background, so that their interference leads to narrow Fano-type features. This principle cannot be explained using effective medium theory (EMT), and builds on a rarely exploited evanescent mode.

Moreover, because the effective index is very high in the slanted cavity, we can create deep subwavelength cavities of a few nanometers. In particular, cavities as small as about 5 nm

can be designed. In addition, we show that these mechanisms remain valid in the presence of losses for the metals.

In Sec. II we present the proposed design. Section III inspects the light behavior using effective medium theory, leading to an incomplete description. In Sec. IV we calculate the correct characteristics, and explain the observed behavior. Finally, in Sec. V we discuss the effect of lossy metals, and Sec. VI concludes.

II. DESIGN

We study the transmission and reflection of light along the parallel direction (so $k_{\perp} = k_y = 0$) of a HMM with a finite section of tilted layers in the middle (Fig. 1). The central tilt section is described by A (the vertical offset), B (the horizontal offset), and L (the parallel length) with $L = \sqrt{A^2 + B^2} = \frac{A}{\sin\theta}$, and θ is the tilt angle.

Because we work in the visible and near-infrared region, we use silver (Ag) as the metal and TiO₂ as the dielectric, which are well known to provide good performances at these frequencies [27–29]. We choose $d_m = 10$ nm for the Ag thickness and $d_d = 20$ nm for the TiO₂ thickness. We use a dispersionless index for TiO₂ with $n_{\text{TiO}_2} = 2.7$ and a Drude model for Ag:

$$\varepsilon_{\text{Ag}} = 1 - \frac{\omega_p^2}{\omega^2 + i\omega\gamma}, \quad (1)$$

with $\omega_p = 1.26 \times 10^{16}$ Hz the plasma frequency and γ the collision frequency that we fix equal to zero; we examine the influence of losses in Sec. V.

We work in the regime where only one propagating Bloch mode exists in the HMM, hence the wavelength is larger than 600 nm in our case. We excite the structure from Fig. 1 with this propagating mode from the left and look at its reflectance and transmittance for a Bloch momentum $k_y = 0$.

In the next section we study this structure using an effective medium theory, which will show its limits to describe such systems.

III. EFFECTIVE MEDIUM THEORY

For a uniaxial multilayer using effective medium theory, the dispersion relation for TM waves (transverse magnetic,

*fabio.vaianella@umons.ac.be

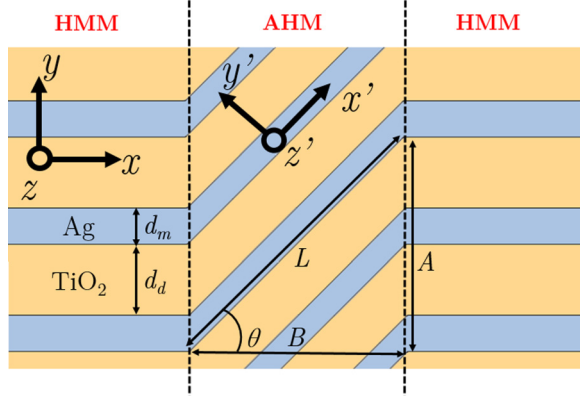


FIG. 1. A multilayer HMM with a tilted section in the middle. The modes are excited from the left. The structure is divided into three parts along the x direction: Two identical HMMs on the left and right and an asymmetrical HMM (or AHM) in the center.

magnetic field along z direction) is [30,31]

$$\frac{k_{\parallel}^2}{\varepsilon_{\perp}} + \frac{k_{\perp}^2}{\varepsilon_{\parallel}} = k_0^2, \quad (2)$$

where k_{\parallel} (k_{\perp}) is the wave vector in the direction parallel (perpendicular) to the layers. The permittivity in the parallel and normal directions depends only on the permittivity of the constitutive materials and their filling fraction:

$$\varepsilon_{\parallel} = f\varepsilon_m + (1-f)\varepsilon_d, \quad (3)$$

$$\varepsilon_{\perp} = \frac{\varepsilon_m \varepsilon_d}{f\varepsilon_d + (1-f)\varepsilon_m}, \quad (4)$$

where ε_{\parallel} and ε_{\perp} are the components of the permittivity in the parallel and perpendicular directions, ε_m and ε_d are the permittivity of the metal and the dielectric, respectively, and f is the metal filling fraction.

For the used wavelength regime, these materials turn out to be very particular anisotropic media, namely HMMs, where components of the diagonalized permittivity tensor have opposite sign, and Eq. (2) is thus the equation of a hyperbola. Consequently, the HMM can support propagating modes with extremely large wave vectors. We note, however, that this equation also has other solutions. There is an evanescent mode (imaginary parallel momentum and real perpendicular momentum), and a mode with real parallel momentum and imaginary perpendicular momentum. These modes are often overlooked, because they are accessible only in certain conditions. We show later on that we fulfill the conditions to excite the evanescent mode, and it will play an important role for the cavity mechanism in the next section.

The geometry explained in the previous section can be divided into three different parts (Fig. 1). The left and right parts are “standard” HMMs and are governed by Eq. (2) with $\varepsilon_{\perp} = \varepsilon_y$, $\varepsilon_{\parallel} = \varepsilon_x$, and $k_{\parallel} = k_x$, $k_{\perp} = k_y$.

The central part however is a hyperbolic medium with the optical axis tilted with respect to the x direction. In the literature these HMMs with tilted optical axis are sometimes referred to as asymmetric hyperbolic metamaterials (AHMs) [32,33].

The AHM part of Fig. 1 is also governed by Eq. (2), but with $\varepsilon_{\perp} = \varepsilon_{y'}$, $\varepsilon_{\parallel} = \varepsilon_{x'}$ and $k_{\parallel} = k_{x'}$, $k_{\perp} = k_{y'}$. Even if the thicknesses of the Ag and TiO₂ layers in the central part change ($d'_m = d_m \cos \theta$ and $d'_d = d_d \cos \theta$), we still have the same $\varepsilon_x = \varepsilon_{x'}$ and $\varepsilon_y = \varepsilon_{y'}$, because Eqs. (3) and (4) only depend on the filling fraction f , which remains the same.

Using a coordinate transformation Eq. (2) in the AHM becomes, in the main coordinates,

$$k_x^{(1,2)} = \frac{k_y \varepsilon_{xy} \pm \sqrt{(\varepsilon_{xy}^2 - \varepsilon_{xx} \varepsilon_{yy})(k_y^2 - k_0^2 \varepsilon_{xx})}}{\varepsilon_{xx}}, \quad (5)$$

with the solution $k_x^{(1)}$ corresponding to the sign “+” in the formula for mode propagating towards smaller x and $k_x^{(2)}$ to the sign “−” for waves propagating towards larger x . Note that in our case of normal incidence, $k_x^{(1)}$ and $k_x^{(2)}$ are equal in magnitude. ε_{xx} , ε_{xy} , and ε_{yy} are the permittivity components of the AHM in the main coordinates, which are obtained by applying a rotation matrix to the diagonal permittivity tensor in the tilted coordinates:

$$\bar{\varepsilon} = \mathcal{R}(\theta) \bar{\varepsilon}' \mathcal{R}(\theta)^T = \begin{pmatrix} \varepsilon_{xx} & \varepsilon_{xy} \\ \varepsilon_{xy} & \varepsilon_{yy} \end{pmatrix}, \quad (6)$$

with $\mathcal{R}(\theta)$ the matrix of rotation around the z axis and $\bar{\varepsilon}' = \begin{pmatrix} \varepsilon_x & 0 \\ 0 & \varepsilon_y \end{pmatrix}$ the permittivity tensor in the tilted coordinates. This leads to

$$\varepsilon_{xx} = \varepsilon_{x'} \cos^2 \theta + \varepsilon_{y'} \sin^2 \theta, \quad (7)$$

$$\varepsilon_{xy} = (\varepsilon_{x'} - \varepsilon_{y'}) \cos \theta \sin \theta, \quad (8)$$

$$\varepsilon_{yy} = \varepsilon_{x'} \sin^2 \theta + \varepsilon_{y'} \cos^2 \theta. \quad (9)$$

For zero momentum in the y direction (i.e., $k_y = 0$), the momentum in the x direction is different in the HMMs ($k_x = \sqrt{\varepsilon_y} k_0$) and in the AHM ($k_x = \frac{\sqrt{(\varepsilon_{xy}^2 - \varepsilon_{xx} \varepsilon_{yy})(-k_0^2 \varepsilon_{xx})}}{\varepsilon_{xx}}$), leading to reflection at the interfaces. Thus the introduced design functions as a cavity structure of width B .

Now that we have defined the effective permittivity components in the HMM and AHM parts, we can easily calculate numerically the scattering characteristics of the structure with the different parts replaced by homogeneous blocks with these effective parameters. The reflectance of light as a function of the tilt angle θ and the length L at a wavelength $\lambda_0 = 700$ nm is shown in Fig. 2.

We observe two distinct behaviors above and below a transition tilt angle of about $\theta_t \approx 21^\circ$. This phenomenon can be understood by looking at the isofrequency contours of the HMM and the AHM section, respectively (Fig. 3).

Blue curves correspond to the isofrequency contour of propagating modes, thus with real components for the x and y momenta (therefore, real part of momenta is plotted). Green curves correspond to evanescent modes with imaginary momentum components in both directions (therefore, imaginary part of momenta is plotted). Red curves correspond to modes with real x momentum and imaginary y momentum (therefore, the real part of the momentum is plotted on the abscissa and the imaginary part is plotted on the ordinate). Note that the isofrequency contours of Fig. 3(b) are just the isofrequency contours of Fig. 3(a) rotated by 45° .

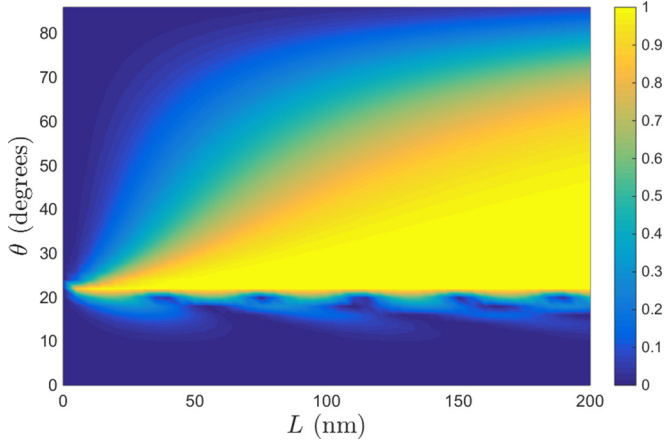


FIG. 2. Reflectance versus tilt length L and angle θ using effective medium theory.

The conservation of the momentum in the transverse direction ($k_y = 0$) imposes in the tilted coordinates (x', y'):

$$k_y = k'_x \sin \theta + k'_y \cos \theta = 0 \quad (10)$$

so

$$k'_x \sin \theta = -k'_y \cos \theta \quad (11)$$

and thus, the mode evanescent in the y' direction and propagating in the x' direction (red curves in Fig. 3) inside the AHM cannot be excited because Eq. (11) cannot be fulfilled. The mode evanescent in all directions (green curves in Fig. 3) and the propagating one (blue curves in Fig. 3) however can fulfill Eq. (11) and can be excited for normal incidence ($k_y = 0$).

The orange arrow in Fig. 3(a) shows the incident momentum inside the HMM. From Fig. 3(b) we see that transverse momentum conservation [the orange arrow in Fig. 3(b) needs to be horizontal] requires that only one mode at a time is excited inside the AHM. The latter mode is either propagating (blue) or evanescent (green), in function of the tilt angle.

The transition angle θ_t between the two regimes is determined by the asymptote of the hyperbolic contours (the

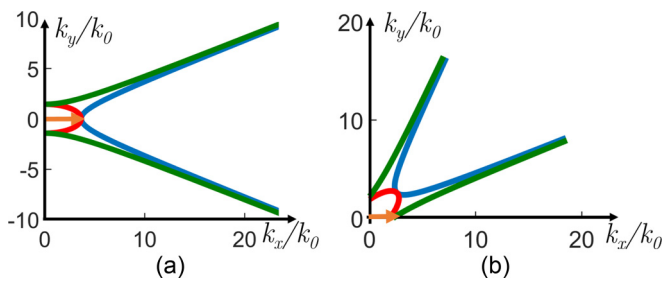


FIG. 3. Isofrequency contours (a) in the HMM and (b) in the AHM for a tilt angle of 45° with EMT, for $\lambda_0 = 700$ nm. Blue curve corresponds to propagating waves, green curve corresponds to evanescent waves, and red curve corresponds to propagating wave in the x direction and evanescent in the y direction. The orange arrow in (a) indicates the input wave vector, in (b) the dominant (green) mode in the AHM. (a) HMM. (b) AHM.

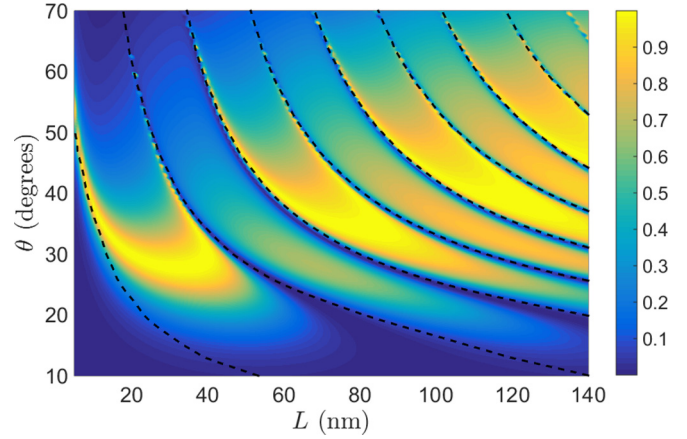


FIG. 4. Exact reflectance in function of θ and L . Black dashed line corresponds to the eight first orders of the Fabry-Perot constructive interferences. The wavelength is 700 nm.

same asymptote for both blue or green contours), this angle equals

$$\theta_t = \text{atan} \left(\sqrt{\frac{\epsilon_x}{\epsilon_y}} \right) \approx 21.6^\circ \quad (12)$$

at $\lambda_0 = 700$ nm.

Thus, below θ_t only a propagating mode (orange arrow touches blue curve) is excited inside the AHM, so the lobes in the lower part of Fig. 2 are Fabry-Perot resonances of the cavity. The fairly weak reflectance of the lobes is typical of Fabry-Perot cavities with low reflection at each interface, which is the case for small tilt angles.

Above θ_t only the evanescent mode (orange arrow touches green curve) is excited in the AHM, leading to the absence of Fabry-Perot fringes. Furthermore, the reflectance increases monotonously with $B (= L \cos \theta)$, because the mode amplitude decreases exponentially with the length of propagation.

In the next section we show that this EMT description is actually incomplete, and only provides for qualitative trends compared to the exact simulations.

IV. RIGOROUS CALCULATIONS AND ANALYSIS

We employ the commercial finite-element software COMSOL Multiphysics 5.2 to calculate the exact propagation through the structure (Fig. 1), with slightly rounded corners to avoid hotspots. The reflectance in function of the tilt angle θ and the parallel propagation length L is shown in Fig. 4. The same lobelike behavior as with EMT below θ_t is present, but the behavior above θ_t is completely different.

In order to understand this difference, we need to take into account the exact dispersion relation obtained by solving Maxwell's equations and applying Bloch's theorem [13,34]

$$\cos(k_y D) = \frac{(\kappa_d \epsilon_m + \kappa_m \epsilon_d)^2}{4\kappa_d \kappa_m \epsilon_d \epsilon_m} \cosh(\kappa_d d_d + \kappa_m d_m) - \frac{(\kappa_d \epsilon_m - \kappa_m \epsilon_d)^2}{4\kappa_d \kappa_m \epsilon_d \epsilon_m} \cosh(\kappa_d d_d - \kappa_m d_m), \quad (13)$$

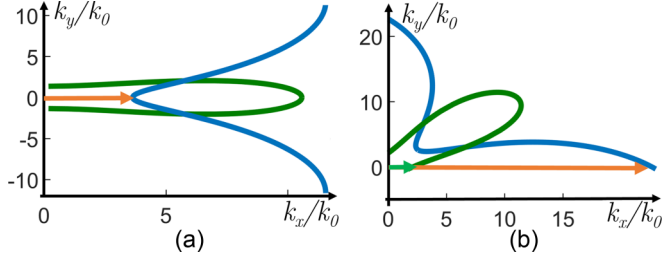


FIG. 5. Exact isofrequency contours (a) in the HMM and (b) in the AHM for a tilt angle of 45° in the first Brillouin zone for $\lambda_0 = 700$ nm. Blue curves correspond to propagating waves and green curves correspond to evanescent waves. Conservation of the transverse wave vector is illustrated by the orange and green arrows. (a) HMM. (b) AHM.

with $D = d_m + d_d$ the period and $\kappa_{d,m} = \sqrt{k_x^2 - k_0^2 \epsilon_{d,m}}$ the decay coefficients in the dielectric and metallic layers, respectively. This dispersion relation is also valid in the AHM, by replacing (k_x, k_y) with (k'_x, k'_y) , $d_{d,m}$ with $d'_{d,m} = d_{d,m} \cos \theta$, and D with $D' = D \cos \theta$. Combining Eq. (13) with the transverse momentum conservation condition [Eq. (11)] in the AHM, we finally arrive at

$$\begin{aligned} \cos(k'_x D' \tan \theta) &= \frac{(\kappa_d \epsilon_m + \kappa_m \epsilon_d)^2}{4\kappa_d \kappa_m \epsilon_d \epsilon_m} \cosh(\kappa_d d'_d + \kappa_m d'_m) \\ &\quad - \frac{(\kappa_d \epsilon_m - \kappa_m \epsilon_d)^2}{4\kappa_d \kappa_m \epsilon_d \epsilon_m} \cosh(\kappa_d d'_d - \kappa_m d'_m). \end{aligned} \quad (14)$$

The main conclusion is that two modes satisfy this equation *at the same time* for all tilt angles θ : an evanescent one and a propagating one. This result is consistent with the rigorously simulated isofrequency contours (Fig. 5), where the blue curve represents the propagating mode and the green curve the evanescent mode.

The orange arrow in Fig. 5(a) shows the incident momentum inside the HMM. In Fig. 5(b), two horizontal arrows are needed to represent the momentum of the two excited modes inside the AHM. The orange arrow represents the momentum of the propagating mode and the green arrow represents the momentum of the evanescent mode.

The first important difference with the EMT contours of Fig. 3 is that the evanescent wave contour (green contours), which was an open curve, is now a closed curve for the exact calculations of Fig. 5. Second, because the structure is periodic, all the information is encoded in the first Brillouin zone, thus the isofrequency contour of the propagating wave (blue curves) is also periodic and is not limited by asymptotes, in contrast with the EMT contours.

For these reasons, inside the AHM, an evanescent and a propagating mode are always excited together. The interferences between these two modes inside the AHM cavity are responsible for the Fano resonances appearing in Fig. 4. Indeed, Fano resonances can be described as arising from the interference between a slowly varying background (here the evanescent wave) and a resonant process (here the Fabry-Perot oscillations of the propagating mode).

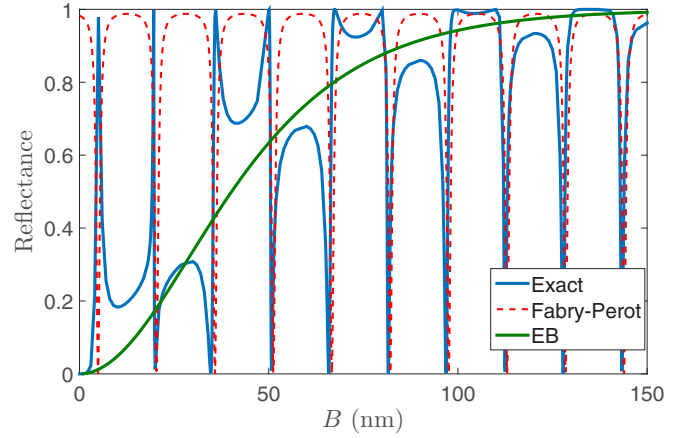


FIG. 6. Comparison between the exact calculation of the reflectance (blue solid curve) and the slowly varying background of the evanescent mode (green solid curve) and the Fabry-Perot oscillations of the propagating mode (red dashed curve) for $\theta = 45^\circ$ at $\lambda_0 = 700$ nm.

The Fano nature is more visible in Fig. 6 (blue curve), which shows the reflectance for an angle $\theta = 45^\circ$ as a function of the width B of the cavity. Figure 6 further illustrates the cavity principle in detail: the Fabry-Perot oscillations of the propagating mode (red dashed curve) and the slowly increasing evanescent background (green curve) are shown separately. Both reflectance curves are obtained using a transfer matrix method under the hypothesis of an isotropic medium (a good approximation for normal incidence) as

$$R = |r|^2 = \left| \frac{r_{\text{HA}} + r_{\text{AH}} \exp(2ik_x B + \varphi)}{1 + r_{\text{HA}} r_{\text{AH}} \exp(2ik_x B + \varphi)} \right|^2, \quad (15)$$

with r_{HA} and r_{AH} the Fresnel coefficients of the propagating (evanescent) mode for the HMM-AHM and AHM-HMM interfaces, k_x the wave vector in the x direction of the propagating (evanescent) mode, and φ a fitted phase term.

The exact reflectance thus arises from the interference of these two phenomena (leading to the blue curve). When the

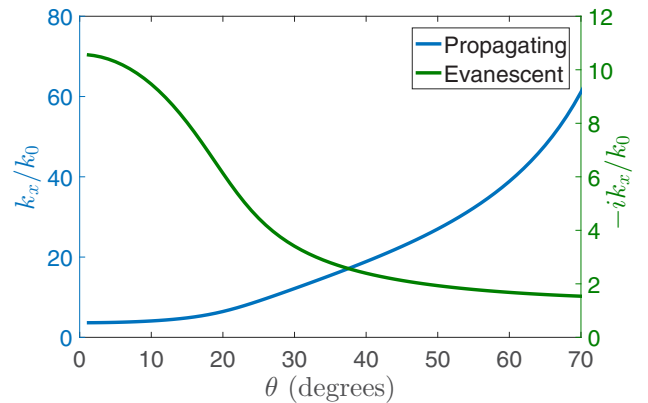


FIG. 7. Momentum in the x direction k_x inside the AHM in function of the tilt angle for $k_y = 0$. Blue curve and axis represent the propagating mode, green curve and axis represent the evanescent mode.

cavity length B becomes larger, the effect of the evanescent mode disappears, as its resulting reflectance (green curve) tends to 1, as the mode decays and does not manage to transmit. Then the characteristic only consists of typical Fabry-Perot oscillations from the propagating mode. For smaller lengths we obtain the typical asymmetric double-peak (maximum-minimum or vice versa) Fano characteristics.

Black dashed lines in Fig. 4 show the good correspondence between the Fano resonances and the Fabry-Perot peaks of the propagating mode; the latter are plotted using a typical phase-matching round-trip relation

$$2k_x(\theta)B + 2\varphi(\theta) = 2\pi m, \tag{16}$$

with m an integer indicating the order, $\varphi(\theta)$ the phase change at each interface obtained by fitting, and $k_x(\theta)$ the wave vector in the x direction for $k_y = 0$ obtained from Eq. (14) (and using $k_x = k'_x \cos \theta - k'_y \sin \theta$). The momentum in the x direction for the evanescent and propagating modes is shown in Fig. 7.

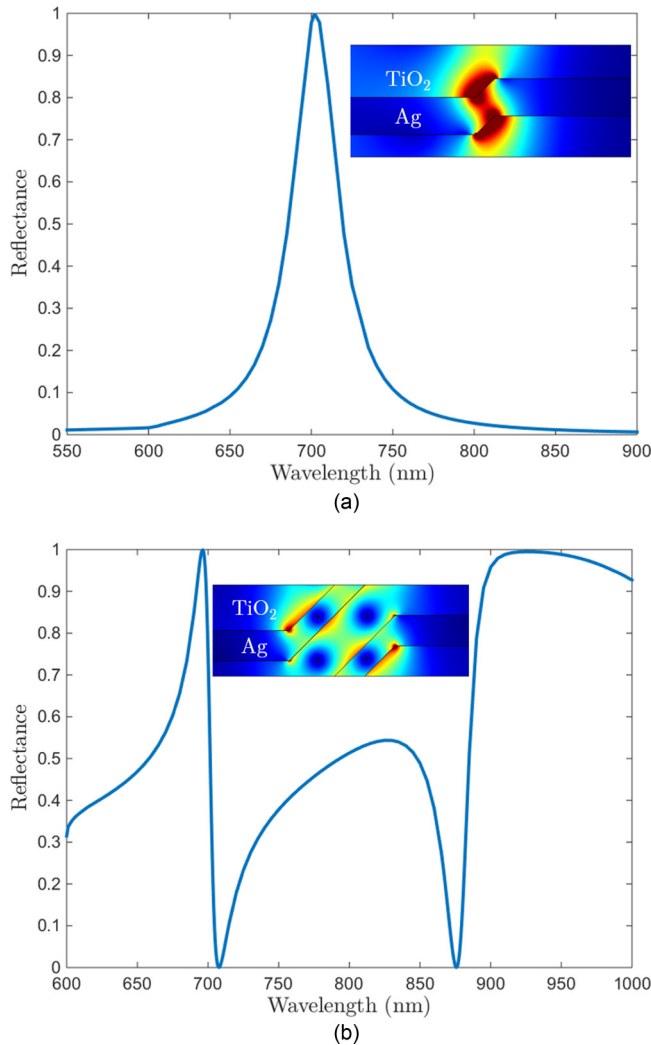


FIG. 8. Reflectance spectra with (a) $A = 5$ nm, $B = 5$ nm. (b) $A = 35$ nm, $B = 35$ nm. Insets show the magnitude of the electric field at the resonance wavelength $\lambda_0 = 700$ nm for a single unit cell of the periodic stacks.

The very high value of the mode inside the cavity leads to the possibility to create very compact cavities, on the order of 5 nm width for $\theta = 45^\circ$ (first peak in Fig. 6). For the first order ($m = 1$) the reflectance shows a single peak, so no asymmetric double-peak characteristic, which is similar to other contexts, such as a cavity placed on the side of a wave guide [35]. The latter effect is intuitively acceptable as the evanescent mode background (the “direct” channel) has a very large transmission for very thin cavities.

The resonance shapes are also present in the spectra of the structure. We show these spectra in two cases for $\theta = 45^\circ$, with a reflectance peak for $A = 5$ nm, $B = 5$ nm [first order resonance, Fig. 8(a)], and with asymmetric Fano shapes for $A = 35$ nm, $B = 35$ nm [third order resonance for $\lambda_0 = 700$ nm, second order for $\lambda_0 = 885$ nm, Fig. 8(b)].

The insets of Fig. 8 presents the magnitude of the electric field at the first order resonance [inset of Fig. 8(a)] and third order resonance [inset of Fig. 8(b)] for the wavelength $\lambda_0 = 700$ nm. As we can expect, the first order resonance does not present a node in the cavity and the third order profile indicates two nodes. The field inside the cavity for the first order resonance is quite large, so one needs to pay attention to losses, this is discussed in the next section.

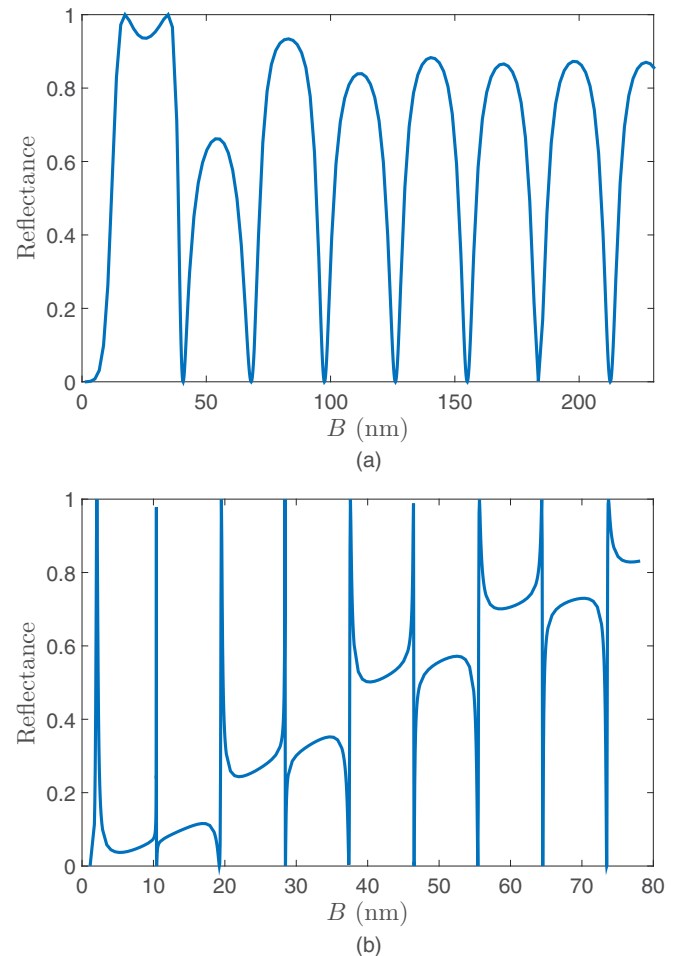


FIG. 9. Reflectance for specific configurations at $\lambda_0 = 700$ nm: (a) $\theta = 30^\circ$. (b) $\theta = 60^\circ$.

The reflectance for two specific tilt angles is presented in Fig. 9, showing that cavity engineering is possible in the regime where hyperbolic modes are supported. For an angle $\theta = 30^\circ$ and $\lambda_0 = 700$ nm [Fig. 9(a)], the green curve of the isofrequency contour of Fig. 5(b) indicates that the imaginary part of the momentum of the evanescent mode is fairly high, which is true for small θ (see also Fig. 7). This explains why the asymmetric Fano resonances disappear rapidly, and quickly lead to standard Fabry-Perot features.

For $\theta = 60^\circ$ and $\lambda_0 = 700$ nm [Fig. 9(b)] the imaginary part for the evanescent mode is low enough to allow for the existence of Fano resonances over a large range of cavity widths (see also Fig. 7). Moreover, as the reflection of the propagating mode at each HMM-AHM interface is larger (because of the larger effective index, see Fig. 7), the peaks are narrower than for the smaller tilt angle [e.g., Fig. 9(a)]. In the next section we introduce losses in the metal and proceed with the same kind of analysis.

V. LOSS EFFECT

Here we use a Drude model with loss for the metal. The collision frequency in Eq. (1) is now $\gamma = 0.5 \times 10^{14}$ Hz, which fits well with experimental measurements [10,36].

Unlike the lossless model, modes with purely real or purely imaginary propagation constant no longer exist. However, the mainly evanescent and propagating modes still exist (if losses are not too large) and are excited with the provision of momentum conversation [Eq. (11)]. Furthermore, in order to show the same Fano mechanism as in the previous section, the modal parameters should obey certain conditions. Specifically, the propagating mode should have a large real part and small imaginary part of the modal refractive index in the x direction, whereas the evanescent mode should have an imaginary part of the mode index in the x direction in the range between around 1 and 2 (above 2 the Fano resonances disappear quickly, below 1 the slowly varying background is not effective).

We focus on structures with metal filling fraction $f = \frac{1}{3}$ as in the previous sections. Equation (14) is still valid, so we can calculate the refractive index of the modes inside the AHM. Figures 10 and 11 show the ratio between the real and

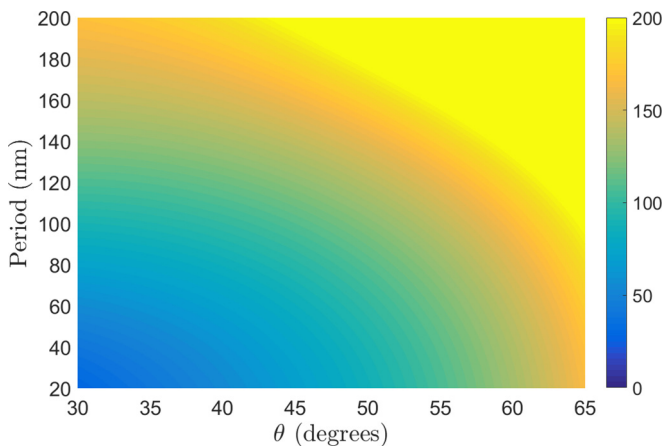


FIG. 10. Ratio between the real and imaginary parts of the refractive index of the propagating mode inside the AHM.

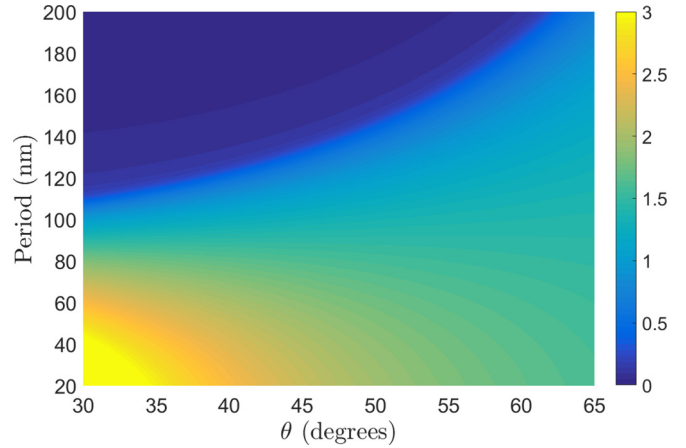


FIG. 11. Imaginary part of the refractive index of the evanescent mode inside the AHM.

imaginary parts of the propagating mode, and the imaginary part of the evanescent mode, respectively. The structure with period of 30 nm and tilt angle of 65° respects the conditions cited above, so we use these parameters for the simulations.

From the field profiles (insets of Fig. 8) we can see hotspots created by sharp corners. These hotspots are critical in the presence of loss and can kill the resonance effect, therefore we limit their influence by replacing sharp corners with sections of 10 nm radius circles.

The reflectance and transmittance in function of the cavity width B is shown in Fig. 12. We still observe the Fano resonances and the extreme sensitivity to small changes in the cavity width. The cavity principle thus remains operational, as the spectrum in Fig. 13 also illustrates. Note that the decrease in transmittance corresponds to an increase in reflectance, so it is an interference effect, and not only due to metal absorption.

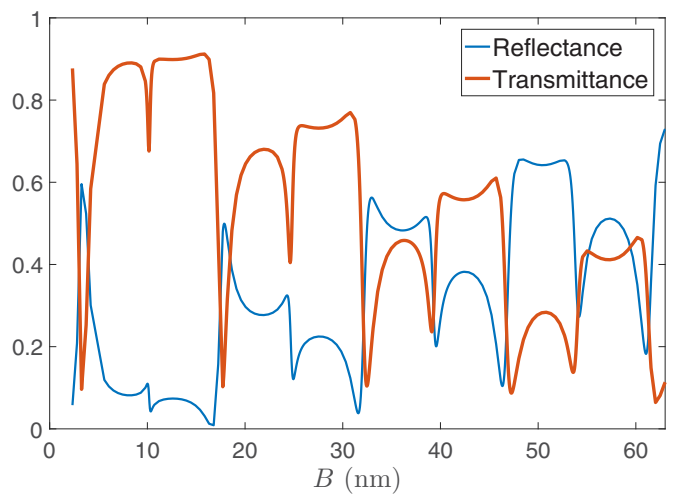


FIG. 12. Reflectance and transmittance with period 30 nm and tilt angle 65° with losses. Blue curve corresponds to the reflectance, red curve to transmittance.

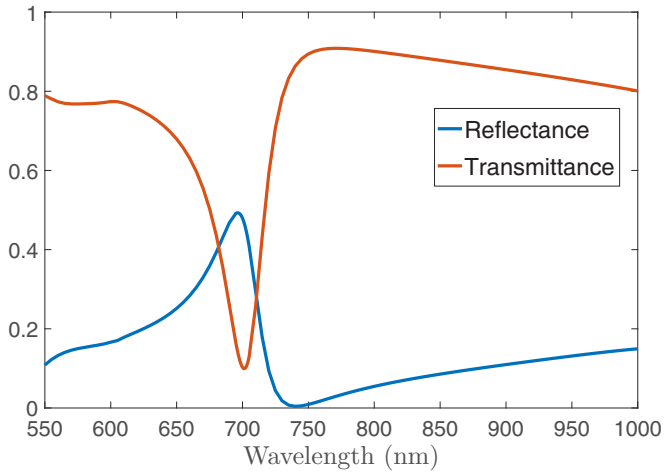


FIG. 13. Reflectance and transmittance spectrum with period 30 nm, tilt angle of 65° , and cavity width $B = 17.7$ nm with losses. Blue curve corresponds to the reflectance, red curve to transmittance.

VI. CONCLUSION

We show that a multilayer structure with a tilted section in the middle corresponds to a cavity made of an asymmetric

hyperbolic metamaterial. Inside this cavity, for normal incidence ($k_y = 0$), a propagating mode and an evanescent mode are always excited. The propagating mode is responsible for Fabry-Perot oscillations, while the evanescent mode “direct” channel leads to a slowly varying background.

The interference between these two modes leads to so-called Fano resonances with asymmetric shapes. Furthermore, effective medium theory cannot explain the existence of these resonances, as it only predicts a single mode at a time, either propagating or evanescent.

The relatively large effective index inside the cavity offers the possibility to create very compact extremely subwavelength cavities. Furthermore, the specific characteristic can be tailored, either presenting total transmittance or total reflectance at resonance, or an asymmetric spectrum.

For structures with metal losses these Fano resonances still exist. This bimodal interference mechanism thus offers new practical possibilities, for instance in the domain of sensing applications.

ACKNOWLEDGMENTS

This work is supported by the Belgian Science Policy Office under the project “Photonics@be” (P7-35) and by the Fonds pour la Formation à la Recherche dans l’Industrie et dans l’Agriculture (FRIA) in Belgium.

-
- [1] V. Shalaev and W. Cai, *Optical Metamaterials: Fundamentals and Applications* (Springer, Berlin, 2010).
 - [2] M. Skorobogatiy, *Nanostructured and Subwavelength Waveguides* (John Wiley and Sons, New York, 2012).
 - [3] B. Li, Y. He, and S. He, *Appl. Phys. Express* **8**, 082601 (2015).
 - [4] A. V. Kildishev, A. Boltasseva, and V. M. Shalaev, *Science* **339**, 1232009 (2013).
 - [5] T. Galfsky, H. N. S. Krishnamoorthy, W. Newman, E. E. Narimanov, Z. Jacob, and V. M. Menon, *Optica* **2**, 62 (2015).
 - [6] A. A. Orlov, S. V. Zhukovsky, I. V. Iorsh, and P. A. Belov, *Photon. Nanostruct.* **12**, 213 (2014).
 - [7] W. D. Newman, C. L. Cortes, and Z. Jacob, *J. Opt. Soc. Am. B* **30**, 766 (2013).
 - [8] O. D. Miller, S. G. Johnson, and A. W. Rodriguez, *Phys. Rev. Lett.* **112**, 157402 (2014).
 - [9] K. V. Sreekanth, T. Biaglow, and G. Strangi, *J. Appl. Phys.* **114**, 134306 (2013).
 - [10] X. Yang, J. Yao, J. Rho, X. Yin, and X. Zhang, *Nat. Photon.* **6**, 450 (2012).
 - [11] D. Keene and M. Durach, *Opt. Express* **23**, 18577 (2015).
 - [12] S. Feng, J. Elson, and P. Overfelt, *Opt. Express* **13**, 4113 (2005).
 - [13] A. A. Orlov, P. M. Voroshilov, P. A. Belov, and Y. S. Kivshar, *Phys. Rev. B* **84**, 045424 (2011).
 - [14] S. V. Zhukovsky, A. A. Orlov, V. E. Babicheva, A. V. Lavrinenko, and J. E. Sipe, *Phys. Rev. A* **90**, 013801 (2014).
 - [15] S. V. Zhukovsky, O. Kidwai, and J. E. Sipe, *Opt. Express* **21**, 14982 (2013).
 - [16] S. V. Zhukovsky, A. Andryieuski, J. E. Sipe, and A. V. Lavrinenko, *Phys. Rev. B* **90**, 155429 (2014).
 - [17] F. Vaianella and B. Maes, *Phys. Rev. B* **93**, 165417 (2016).
 - [18] J. Elser, R. Wangberg, V. A. Podolskiy, and E. E. Narimanov, *Appl. Phys. Lett.* **89**, 261102 (2006).
 - [19] N. Vasilantonakis, M. E. Nasir, W. Dickson, G. A. Wurtz, and A. V. Zayats, *Laser Photon. Rev.* **9**, 345 (2015).
 - [20] C. Wu, A. Salandrino, X. Ni, and X. Zhang, *Phys. Rev. X* **4**, 021015 (2014).
 - [21] Z. Huang and E. E. Narimanov, *Opt. Express* **21**, 15020 (2013).
 - [22] M. Hasan and I. Iorsh, Interaction of light with a hyperbolic cavity in the strong-coupling regime with Fano resonance, in *2015 Days on Diffraction (DD 2015), 25-29 May 2015, St. Petersburg, Russia* (IEEE, 2015) pp. 140–145.
 - [23] A. E. Miroshnichenko, S. Flach, and Y. S. Kivshar, *Rev. Mod. Phys.* **82**, 2257 (2010).
 - [24] S. Fan and J. D. Joannopoulos, *Phys. Rev. B* **65**, 235112 (2002).
 - [25] I. V. Iorsh, I. V. Shadrivov, P. A. Belov, and Y. S. Kivshar, *Phys. Rev. B* **88**, 195422 (2013).
 - [26] B. Luk’yanchuk, N. I. Zheludev, S. A. Maier, N. J. Halas, P. Nordlander, H. Giessen, and C. T. Chong, *Nat. Mater.* **9**, 707 (2010).
 - [27] C. L. Cortes, W. Newman, S. Molesky, and Z. Jacob, *J. Opt.* **14**, 063001 (2012).
 - [28] B. Dastmalchi, P. Tassin, T. Koschny, and C. M. Soukoulis, *Adv. Opt. Mater.* **4**, 177 (2016).
 - [29] P. Tassin, T. Koschny, M. Kafesaki, and C. M. Soukoulis, *Nat. Photon.* **6**, 259 (2012).

- [30] A. Poddubny, I. Iorsh, P. Belov, and Y. Kivshar, *Nat. Photon.* **7**, 948 (2013).
- [31] X. Ni, S. Ishii, M. D. Thoreson, V. M. Shalaev, S. Han, S. Lee, and A. V. Kildishev, *Opt. Express* **19**, 25242 (2011).
- [32] I. S. Nefedov, C. A. Valagiannopoulos, S. M. Hashemi, and E. I. Nefedov, *Sci. Rep.* **3**, 2662 (2013).
- [33] A. D. Boardman, P. Egan, and M. McCall, *EPJ Appl. Metamater.* **2**, 1 (2015).
- [34] G. Rosenblatt and M. Orenstein, *Opt. Express* **19**, 20372 (2011).
- [35] B. Maes, P. Bienstman, and R. Baets, *J. Opt. Soc. Am. B* **22**, 1778 (2005).
- [36] P. B. Johnson and R. W. Christy, *Phys. Rev. B* **6**, 4370 (1972).